Takahiro Abe[1], Go Iwahana[2,3], Takeo Tadono[4], and Yoshihiro Iijima[1]

[1]Graduate School of Bioresources, Mie University, Tsu, JAPAN.

[2]Internatinal Arctic Research Center, University of Alaska Fairbanks, Fairbanks, USA.

[3]Arctic Research Center, Hokkaido University, Sapporo, JAPAN.

[4]Earth Observation Research Center, Japan Aerospace Exploration Agency, Tsukuba, JAPAN.

Corresponding author: Takahiro Abe (abe@bio.mie-u.ac.jp)

Key Points:

- Ground subsidence was primarily associated with the severity of forest fires, and slope orientation was likely an additional factor.
- Seasonal frost heave measured by InSAR corresponded to seasonal change of summer precipitation.
- Existing phase change expansion model could not explain observed seasonal displacement quantitatively.

Abstract

Forest fires significantly impact permafrost degradation in the subarctic regions. However, inter-annual and seasonal variations in surface deformation due to permafrost thawing in burned areas were poorly understood. Measuring the ground surface displacement in fire scars helps us understand the freeze–thaw dynamics of near-surface ground and predict the future state, particularly in ice-rich permafrost regions. This study used the L- and C-band interferometric synthetic aperture radar (InSAR) technique to reveal inter-annual subsidence and seasonal thaw settlement/frost heave in a fire scar near Mayya, Sakha Republic in Eastern Siberia burned in 2013. We found that the cumulative subsidence was up to 7 cm between 2014 and 2020, most of which had occurred by 2016. The magnitude of seasonal thaw settlement and frost heave varied each year from 2017 to 2020 after the fire, but the inter-annual change in frost heave corresponded to the temporal variation in precipitation during the thawing season from 2017 to 2020. This suggests that the precipitation amount during the thawing season is related to the magnitude of segregation–ice formation in the sediments, which determines the frost heave amount. The observed seasonal displacements could not be quantitatively explained by models inferred from the Stefan's equation and volume changes associated with ice–water phase change. This implies that other models associated with segregated ice (ice lens) formation/thaw are required to explain the observed seasonal displacement.

Plain Language Summary

Forest fires in permafrost regions significantly affect regional landscape changes and ecosystems through permafrost degradation and subsequent ground defor-

mation. However, the number of observations of post-forest fire surface displacement is extremely limited. We calculated surface displacement in a fire scar in Eastern Siberia from spaceborne radar images captured using Interferometric Synthetic Aperture Radar (InSAR). Our observed data will help us understand permafrost degradation processes in forest fire scars.

1 Introduction

Recent climate change has increased the number of wildfires in Arctic and subarctic (boreal) regions, which has significantly impacted on permafrost conditions (Gibson et al., 2018; Holloway et al., 2020; Zhang et al., 2015). Wildfires do not directly thaw permafrost, but trigger their degradation through the loss of surface vegetation and organic layers (Yoshikawa et al., 2003), which play an important role in preventing solar radiation shielding. Regardless of the cause of wildfires, the loss of vegetation and organic layers has both immediate and long-term effects on permafrost environments through changes in the surface energy balance, ground thermal and hydrological regimes, and soil and aquatic biogeochemistry (Holloway et al., 2020). Furthermore, the organic carbon trapped in permafrost regions is estimated to be twice that in the current atmosphere, and permafrost thawing may further enhance global warming (Mack et al., 2011; Schuur et al., 2015).

Central Yakutia (Figure 1a) is underlain by ice-rich continuous permafrost (Brown et al., 2002). Recently, topographic changes and lake formation due to thermokarst have increased (Fedorov et al., 2014; Ulrich et al., 2017). Thermokarst is a characteristic process that results from ice-rich permafrost thawing and massive underground ice melting (Czudek & Demek, 1970; van Everdingen 2005). Heterogeneous surface subsidence occurs in the initial stage of thermokarst, which is related to ice volume loss (Ulrich et al., 2014). In the last three decades, the mean air temperature has increased by apporoximately 3 ℃ (Desyatkin, Fedrov, et al., 2021) and, in particular, high temperatures and intensive precipitation in the late 2000s are considered to have caused thermokarst progression and forest mortality (Iijima et al., 2010; Fedorov et al., 2014). In the continuous permafrost zone, including Central Yakutia, open and disturbed areas including wildfire scars on ice-rich permafrost, are at the risk of degradation (Fedorov et al., 2017). Therefore, wildfire scars are the focus of permafrost degradation in the Arctic region (Yanagiya and Furuya, 2020). Despite the significant impact of wildfires on permafrost, spatial and temporal changes in permafrost degradation in fire scars are not well understood due to the lack of quantitative observation data.

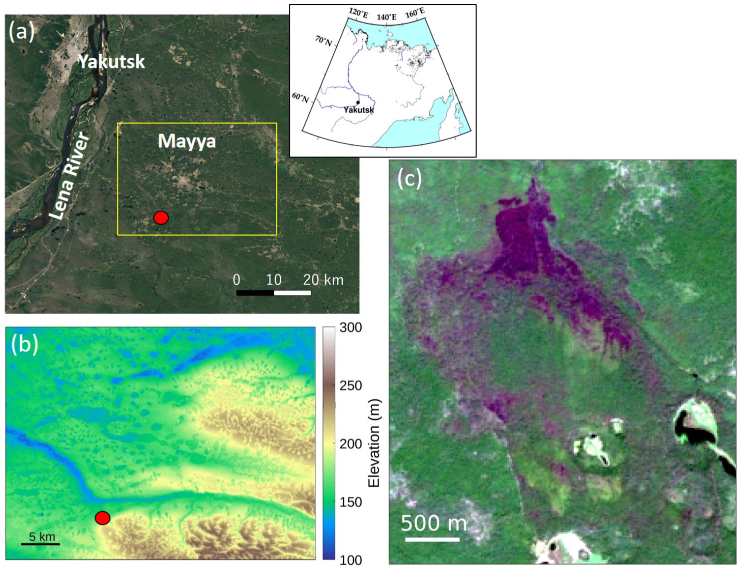

Figure 1. Study area. (a) Enlarged map near Yakutsk in the right bank of Lena River. Yellow rectangle shows the area enlarged in (b). Location of the 2013 forest fire is approximately 10 km far from Mayya (red dot). (b) Elevation map around the study area. (c) Landsat true color image on 18 August, 2013 over the 2013 forest fire area.

Remote sensing techniques are useful for monitoring ground surfaces without conducting field surveys. In particular, interferometric synthetic aperture radar (InSAR) is a powerful tool to investigate surface displacement in fire scars underlain by permafrost (Liu et al., 2014; Iwahana et al., 2016; Molan et al., 2018; Michaelides et al., 2019; Yanagiya and Furuya, 2020; Yanagiya, 2022), while very few studies have used this technique. Yanagiya and Furuya (2020) recently showed spatial and temporal changes in surface displacement after a wildfire in 2014 in Batagay, northeastern Siberia, using the Advanced Land Observing Satellite-2 (ALOS-2) InSAR time-series analysis. They revealed cumulative subsidence of 30 cm from 2015 to 2019 with apparent increases in seasonal thaw settlement and frost heave in the burned areas. This time-series displacement data is very rare and important to better understand permafrost degradation processes in fire scars (Kornei, 2020). However, they did not detail the interannual change in seasonal displacement. Thus, further studies on long-term and seasonal displacements at fire scars are required.

InSAR-based displacement data have been utilized for estimating maximum seasonal thaw depth [active layer thickness (here after ALT)] using the Stefan's equation and an assumption of volume expansion/decrease due to phase change of water within the active layer (Liu et al., 2012; Schaefer et al., 2015). However, these studies did not show whether the observed displacement could be explained by the phase change expansion model; air temperature data were used as a temporal constraint condition for deriving the time-series displacement data. Molan et al. (2018) modeled the ALOS InSAR-based post-wildfire surface subsidence in the Alaskan Yukon River Basin considering a two-layer system of an active layer and an underlying permafrost. Their approach was also based on the expansion model. Furthermore, even though soil moisture is the key parameter of the modeled displacement in the expansion model, no study has focused on how much the moisture is necesary to explain the observed displacement data. Thus, detailed investigations are needed to clarify whether freezing/thawing and subsequent volume expansion/decrease of pre-existing pore water are sufficient to explain the observed ground surface displacement among freeze–thaw processes.

This study has three objectives: First, to reveal the inter-annual ground surface displacement after a few years due to permafrost degradation and estimate the thawed ice volume. This study focused on a forest fire that occurred in 2013 in Mayya (Figures 1a and 1b), Central Yakutia, underlain by continuous ice-rich permafrost. Abe et al. (2020) reported thermokarst subsidence in Mayya using ALOS/ALOS-2 InSAR stacking, indicating that thermokarst-induced ground subsidence in the Mayya region has been ongoing. Therefore, the forest fire in Mayya is a good case for examining the impact of landcover change by fire on permafrost degradation. The second objective is as to examine what controls the seasonal surface displacement. Although ALT is closely related to air temperature, the relationship between ALT and seasonal surface displacement remains unclear. It is important to understand the factors other than air temperature that are related to seasonal surface displacement. The third objective is to investigate whether the observed seasonal displacement could be explained using an existing phase change expansion model. To clarify this, we used the phase change expansion model and soil parameters based on related field surveys to compare the modeled displacement with the InSAR-based observed seasonal displacement. This investigation will help us better understand the physics of seasonal freeze/thaw cycles and the subsequent surface displacement.

2 Study area

Mayya (Figures 1a and 1b) is a rural locality located on the right bank of the Lena River and 40 km southeast of Yakutsk. It is mostly surrounded by boreal forests with larch and pine trees (Figure 1a), although the village was deforested for farming, primarily in the 1970s. Mayya is located on fairly flat ground with ~140 m elevation, and the southern part of the village is higher, with up to 200 m elevation (Figure 1b). Alases, the final geomorphological stage of old thermokarst development (Bosikov, 1991), can be identified by its slightly lower elevation and greenness compared to the surrounding yellow inter-alas meadow (Figure 1b). The long-term averaged ALT in thermokarst-affected areas is 2–3.5 m, while that in intact areas is 1.8–2.7 m in the Mayya region. Mayya represents the residential areas in Central Yakutia with thermokarst development. Abe et al. (2020) first examined the spatial variation of averaged ground subsidence rate in Mayya using ALOS-2 InSAR stacking, and revealed the subsidence rate to be 0.5–2 cm yr^{-1} in the deforested areas, all of where thermokarst-induced polygonal texture were identified. The forest fire studied occurred in June–July 2013 (Figure 1c), approximately 10 km south of Mayya village on the Abalakh terrace of the Lena River (Soloviev, 1959; Ulrich et al., 2017).

3 Data and method

3.1 Identification of fire scar and monitoring vegetation recovery by Landsat multi-spectral images

The normalized burn ratio (NBR) is a useful index for identifing wildfire–affected areas by focusing on vegetation changes. Vegetation is more significant in the near-infrared (NIR) region than that in the shortwave infrared (SWIR) region, whereas fire scars are more significant in the SWIR region. Based on these properties, NBR is defined as (NIR − SWIR) / (NIR + SWIR). The difference in NBRs (dNBR) pre-and post-fire indicates burn severity (Key & Benson, 2006; Miller & Thode, 2007). Generally, a fire with dNBR $>$ 0.66 is regarded as highly severe (Key & Benson, 2006). We calculated dNBR for the 2013 fire using spectral radiance in the Landsat 7 NIR (Band 4; 0.77–0.90 m) and SWIR (Band 7; 2.09–2.35 m) bands (Table 1) to support the identification of the burned area.

In addition to identifying the burned area, we examined vegetation recovery after the fire. The normalized difference vegetation index (NDVI) is defined as (R - NIR) / (R + NIR), where R is a red band. We calculated NDVI between 2013 and 2020 using spectral radiance in the Landsat 8 red (Band 4: 0.64–0.67 m) and near-infrared (Band 5: 0.85–0.88 m) bands (Table 1) to reveal inter-annual NDVI changes after the fire.

Table 1 List of Landsat images used in this study.

Scene ID	Date (dd/mm/yyyy)
Landsat 7	
LE07_L1TP_121017_20120807_20200908_02_T1	07/08/2012
LE07_L1TP_121017_20130810_20200907_02_T1	10/08/2013
Landsat 8	
LC08_L1TP_121017_20130818_20200912_02_T1	18/08/2013
LC08_L1TP_121017_20150808_20200908_02_T1	08/08/2015
LC08_L1TP_120017_20160819_20200906_02_T1	19/08/2016
LC08_L1TP_120017_20170721_20200903_02_T1	21/07/2017
LC08_L1TP_120017_20180809_20200831_02_T1	09/08/2018
LC08_L1TP_120017_20190727_20200827_02_T1	27/07/2019
LC08_L1TP_121017_20200618_20200823_02_T1	18/06/2020

3.2 InSAR analysis and validation using ALOS-2 and Sentinel-1 data

InSAR is a uniquel tool to examine surface displacement using two SAR images at different times with an accuracy of a few centimeters (Hanssen, 2001). InSAR has been used for detecting surface deformations related to permafrost such as seasonal freeze/thaw cycles (e.g., Liu et al., 2010; Short et al., 2011; Daout et al., 2017; Strozzi et al., 2018; Rouyet et al., 2019), thermokarst (Liu et al., 2015; Annotova et al., 2018; Chen et al., 2018; Abe et al., 2020; Iijima et al., 2021), and wildfires (Liu et al., 2014; Iwahana et al., 2016; Molan et al., 2018; Michaelides et al., 2019; Yanagiya & Furuya, 2020; Yanagiya, 2022). L-band InSAR is more suitable than C-and X-band InSAR to examine long-term displacement such as thermokarst subsidence, with respect to coherence (Wang et al., 2017; Strozzi et al., 2018; Abe et al., 2020; Yanagiya & Furuya, 2020; Yanagiya, 2022). On the contrary, C-band SAR Sentinel-1 has performed high-frequency observations over the study area at an interval of 12 or 24 days, which enabled us to investigate seasonal thaw settlement and frost heave. Thus, we also used the Sentinel-1 images to analyze the seasonal displacement.

In this study, L-band SAR obtained from the Phased Array-type L-band Synthetic Aperture Radar (PALSAR)-2 aboard ALOS-2 and C-band SAR from Sentinel-1 images were processed using Gamma software (Wegmüller and Werner, 1997). Six scenes of ALOS-2 stripmap mode 3 (SM3) with 10-m resolution over the fire site in 2014-2020 (Table 2) were used to derive inter-annual changes in ground surface displacement. The revisit interval for ALOS-2 was 14 days, but the observation interval for interferometry over the study area was basically one or two times per year, almost all of which occurred from August to October. In addition, the center frequency of beam F2_6 (the same beam we used) was modifed in June 2015. Therefore, interferometry between the F2_6 data acquired before and after June 1 2015, is undesirable because of the significant coherence decrease (Natsuaki et al., 2016). Thus, we generated interferograms using the data acquired before and after June 1 2015. After checking the interferograms, we regarded one interferogram between 2014 and 2015 (Table 2), which is useful for this study in terms of coherence. Sentinel-1 has collected more than 100 scenes in the interferometric wide swath mode at 5×20 m^2 resolution (Table S1) since November 2016 over the study area. Thus, we processed Sentinel-1 data from April 2017 to March 2021 to derive seasonal changes in surface displacement. The incidence angles of the ALOS-2 and Sentinel-1 SAR images at the fire site were approximately 36°and 33°, respectively. In the datasets used, ALOS-2 and Sentinel-1 illuminated the surface from the west and east, respectively; thus, the signs of sensitivity to the east–west displacement were reversed. The topographically related phase was removed using the ALOS World 3D -30 m- (AW3D30, Takaku et al., 2020).

Table 2 Interferometric paris of ALOS-2 used in the Figure 4. B-perp stand for the distance perpendicular to the line of sight between the positions of the satellite at different times.

Image 1 (dd/mm/yyyy)	Image 2 (dd/mm/yyyy)	B-perp (m)	Span (day)
03/10/2014	02/10/2015	42.5	364

Image 1 (dd/mm/yyyy)	Image 2 (dd/mm/yyyy)	B-perp (m)	Span (day)
02/10/2015	30/09/2016	-101	364
30/09/2016	12/10/2018	127	742
12/10/2018	11/10/2019	-141	364
11/10/2019	17/07/2020	58.8	280
02/10/2015	17/07/2020	-56.3	1750

Our InSAR processing procedures were similar to those used in previous studies (Strozzi et al., 2018; Abe et al., 2020; Yanagiya and Furuya, 2020; Iijima et al., 2021). We generated single-look complex (SLC) data from ALOS-2 level 1.1 data. After performing co-registration between two SLC images, we generated interferograms and selected 11 interferograms, excluding those with the image acquisition period of over four years or with in the same year (Table 2). Goldstein–Werner's adaptive spectral filter with an exponent of 0.7 was applied to smooth the signals (Goldstein and Werner, 1998), and phase unwrapping by minimum cost flow was performed (Costantini, 1998). The spatial resolution after terrain-corrected geocoding projecting onto the UTM coordinate was set to 30 m. InSAR reference points should be set in each interferogram, but there was no information for selecting as a stable ground point in the area. Thus, the averaged phase outside the fire scar in each interferogram was shifted to zero to derive the ground surface displacement in the fire scar relative to the outside of the fire scar.

Tropospheric and ionospheric noises sometimes affect each interferogram, which sometimes introduces significant errors in the extraction of the surface displacement. Our study area is located on a relatively flat fluvial terrace of the Lena River, and the regional climate is semi-arid (annual precipitation apporoximately 250 mm). Thus, we considered the tropospheric effect sufficiently small to be neglected. The effects of ionospheric disturbances are often observed as linear long-wavelength trends. Our analysis area was spatially limited to $\sim 5 \times 5$ km^2, and we modeled and subtracted the trend by fitting a 2D polynomial function.

Although validation using in-situ data such as leveling and/or GNSS is ideal, there are no available data for comparison with the InSAR-based surface displacement, as already mentioned above. Thus, we cross-validated the interferograms using different band and orbit SAR data from ALOS-2 and Sentinel-1, as reported by Yanagiya and Furuya (2020). The ALOS-2 and Sentinel-1 observation frequencies were significantly different over the study area. The ALOS-2 observation frequency of ALOS-2 is one or a few times per year, and we could not generate interferograms showing seasonal displacement for almost all years. On the contrary, Sentinel-1 has performed frequent observations over the area with an interval of 12 days, which has enabled us to calculate seasonal displacement. Even with high-frequency Sentinel-1 acquisitions, we could not obtain coherent interferograms using the data from the early thawing season in April–May, probably due to surface inundation by snowmelt. Therefore, it was quite difficult to derive inter-annual changes in the surface displacement using Sentinel-1 data. Fortunately, there were a few ALOS-2 observations over the area in 2019. Two consecutive ALOS-2 interferograms were generated and compared with stacked Sentinel-1 interferograms for validation (Table 3).

Table 3 Interferometric paris of ALOS-2 and Sentinel-1 used in Figure 6.

Image 1 (dd/mm/yyyy)	Image 2 (dd/mm/yyyy)	B-perp (m)	Span (day)
ALOS-2 interferograms			
07/06/2019	19/07/2019	-74.5	42
19/07/2019	11/10/2019	63.2	84
Sentinel-1 interferograms			
11/06/2019	23/06/2019	-9.9	12
23/06/2019	05/07/2019	85.0	12
05/07/2019	17/07/2019	19.0	12
17/07/2019	29/07/2019	-56.4	12
29/07/2019	10/08/2019	-19.6	12
10/08/2019	22/08/2019	-18.4	12
22/08/2019	15/09/2019	49.1	24
15/09/2019	27/09/2019	122.6	12
27/09/2019	09/10/2019	-161.3	12

3.3 InSAR time-series analysis

To infer long-term temporal changes and cumulative displacements, we performed a small baseline subset (SBAS)-type time-series analysis (Berardino et al., 2002; Schmidt & Bürgmann, 2003; Biggs et al., 2007; Liu et al., 2015; Yanagiya & Furuya, 2020), using 11 high-quality ALOS-2 interferograms. The averaged line-of-sight (LOS) change at each acquisition epoch was estimated without assuming any temporal change models, such as the cyclic function and air temperature data. We also estimated the propagation error from the time-series analysis assuming that each ALOS-2 interferogram contained 0.2 cm errors, which is identical to that reported by Yanagiya and Furuya (2020).

3.4 Modeling seasonal displacement based on the Stefan's equation

To interpret the observed seasonal displacements, we modeled the surface displacement based on the Stefan's equation, a conventional and simple model for calculating the thawing depth from air temperature data (Stefan, 1891). The depth Z(t) at a certain time t is defined as

$$\mathrm{Z}\ (t) = \sqrt{\frac{2knsA(t)}{\mathrm{L}}}\ (1)$$

where k is the thermal conductivity of soil ($\mathrm{W} \cdot \mathrm{m}^{-1} \cdot \mathrm{K}^{-1}$), n is the n-factor indicating the ratio of ground surface temperature to air temperature (Lunardini, 1978; Klene et al., 2001), s is the scaling factor for the conversion of time dimension, A(t) is the accumulated degree days of thawing or freezing (ADDT or ADDF, unit: °C days), is the soil bulk density ($kg \cdot m^{-3}$), is the volumetric water content ($m^3 \cdot m^{-3}$), and L is the specific latent heat of fusion for water ($J \cdot kg^{-1}$). In this study, we calculated the ADDT and ADDF using air temperature data for Yakutsk provided by the National Centers for Environmental Information (NCEI) of the National Oceanic and Atmospheric administration (NOAA) (Menne, Durre, Korzeniewski et al., 2012; Menne, Durre, Vose et al., 2012). The physical constants listed in Table 4 were used in the modeling. Thermal conductivity of unfrozen and frozen soil were set to 1.1 and 1.4, respectively, based on the in-situ results reported by Romanovsky and Osterkamp (2000) and Yershov (1998). The n-factors for summer and winter used were reported by French (2017) and Karunaratne and Burn (2003). Soil bulk density used was reported by Iwahana et al. (2005) and Desyatkin, Filippov et al. (2021).

Table 4 Physical constants used for modeling used in Figure 8 and 9.

Name of Constant	Symbols	Values	Units
Thermal conductivity for unfrozen/frozen soil	k	1.1/1.4	$W\ m^{-1}\ K^{-1}$
n-factor for Summer/Winter	n	0.8/0.32	dimensionless
Scaling factor for time dimension	s	8.64×10^4	dimensionless
Soil bulk density	ρ	1.4×10^3	$Kg\ m^{-3}$
Latent heat of fusion for water	L	3.34×10^5	$J\ Kg^{-1}$
Density of water	ρ_w	1000	$Kg\ m^{-3}$
Density of ice	ρ_i	920	$Kg\ m^{-3}$

Here we assumed that the phase change of water causes the active layer volume during the freezing/thawing season (Liu et al., 2012). Pore water/ice within the active layer turns into ice/water, causing an ~9% volume increase/decrease and the subsequent ground uplift/subsidence, respectively.

The displacement du is calculated as

$du = \frac{\rho_w - \rho_i}{\rho_i}$ dz (2)

where $_w$ and $_i$ represent the density of water and ice, respectively. Assuming that is spatially heterogeneous within the active layer and constant with depth, the surface displacement u(t) at a certain time t is derived from Equations (1) and (2)

u $(t) = \frac{\rho_w - \rho_i}{\rho_i} \sqrt{\frac{2kns\theta A(t)}{\mathrm{L}}}$ (3)

The surface displacement u(t) at a certain time t was rearranged using the coefficient of E as

u $(t) = E\sqrt{A(t)},$ (4)

where E is defined as

$E = \frac{\rho_w - \rho_i}{\rho_i}\sqrt{\frac{2kns\theta}{\mathrm{L}}}$ (5)

E is a time-invariant coefficient, that consists of the products of soil and water properties. Here, E in the freezing and thawing seasons is denoted as $\mathrm{E_f}$ and $\mathrm{E_t}$, respectively.

This equation was used as a temporal constraint condition when deriving the components of seasonal and long-term displacement, and ALT change was obtained from the time-series displacement (Liu et al., 2012; Liu et al., 2015; Schafer et al., 2015; Hu et al., 2018; Michaelides et al., 2019). However, soil parameters in E determined under the constraint have been poorly discussed, although E contains information about ground conditions that explain seasonal surface displacement. In this study, E was first determined using the observed seasonal thaw settlement and frost heave for each year and the differences between the square root of A(t) in the corresponding period (Equation 4). Among the soil properties constituting E, the spatial variation in the volumetric water content ( ) was calculated with other soil properties (Table 4). The properties, except , are assumed to have no spatial variation in the study area and can be used as representative values from previous related studies.

When the surface displaces Δu at the time Δt, is calculated by transforming Equation (5):

$\theta = \left(\frac{\rho_i}{\rho_w - \rho_i}\right)^2 \frac{\mathrm{L}E^2}{2kns}$ (6)

Assuming that is unlikely to be over 60 % in view of in-situ data in Eastern Siberia (Iwahana et al., 2005; Fedorov et al., 2017; Iijima et al., 2017; Abe et al., 2020; Yanagiya, 2022), we replaced the calculated over 60% with 60% and conversely modeled the surface displacement using Equation (3). This manipulation means that the modeled displacement should be equal to the observed displacement when is less than 60%, whereas the modeled and observed displacements should be different when is greater than 60%. The threshold value of 60 % is somewhat arbitrary and may be larger than that of the in-situ observation data. It is important to investigate whether the volumetric change caused by the phase change in soil moisture can explain the ground surface displacement. While soil moisture comprises air and water saturation fractions in the ground and has a vertical distribution, there is no available field data for constraining them. InSAR detects “surface” displacement; thus, we do not consider the vertical distribution of soil properties. Comparing the observed and modeled displacements, we have discussed the seasonal freeze/thaw dynamics in Section 5.3.

4 Results

4.1 Burn severity and recovery of vegetation by Landsat images

Figure 2a shows a map of the dNBR between 2012 and 2013, which indicates the burned area of the 2013 forest fire. Null data with diagonal areas were caused by the sensor failure of Landsat 7 (United States Geological Survey, 2003). The area indicated by the black line was calculated as 5.78 km^2, and the most severe part was located in the center of the northern burned area of 0.22. The areas with negative values correspond to those of the Alas lakes, which are not related to the burned area. The topography of the burned area is shown in Figure 2b. The most severe part of the slope lies on a north-dipping slope of approximately 2 °. The elevation ranges from 160 to 220 m southward.

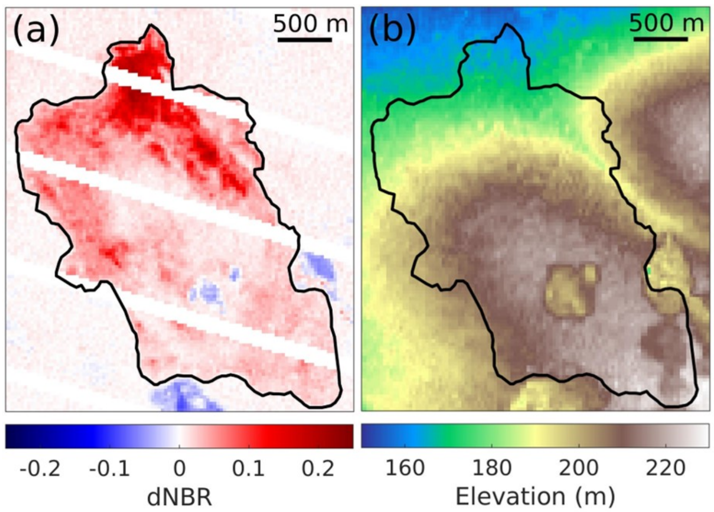

Figure 2. (a) Map of difference in dNBR before and after the fire. Black line shows the identified burn area of the 2013 forest fire. (b) Map of elevation in and around the fire scar.

Figure 3 shows the spatial and temporal changes in NDVI from 2013 to 2020, indicating vegetation recovery after the fire. The NDVI in August 2013 (immediately after the event) is almost 0 in the northern area, which increased over five years to 0.37 in 2018. However, the NDVI decreased up to 0.23 in 2019–2020.

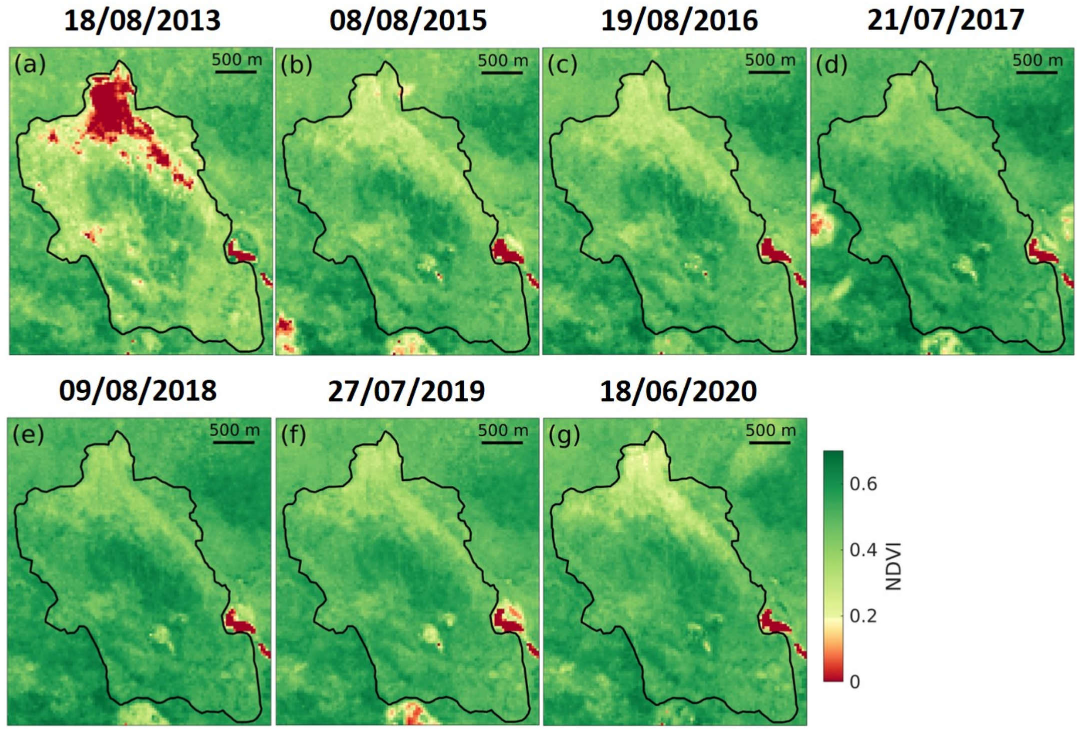

Figure 3. Spatial and temporal changes in NDVI between 2013 and 2020 derived from Landsat 8 multi-spectral images. The black line indicates the burned area identified in Fig. 2a.

4.2 Annual displacement by ALOS-2

The annual LOS changes in the burned area calculating using ALOS-2 interferograms are shown in Figure 4. The interferogram for 2014–2015 shows ~2 cm LOS lengthening in the fire scar (Figure 4a). The following interferogram for 2015–2016 shows that LOS lengthened by ~3 cm (Figure 4b), which is larger than that in the previous year. In the next two years (2016–2018), LOS lengthened by ~1 cm in the north area (Figure 4c). The two interferograms for 2018–2019 (Figure 4d) and 2019–2020 (Figure 4e) indicated almost no LOS changes (~0.5 cm) in the area. The interferogram for 2015–2020 shows that LOS lengthened by ~4.5 cm in the northern burned area (Figure 4f). The spatial distribution of LOS change shows that larger displacements were detected in the northern burned area, followed by that in the middle part.

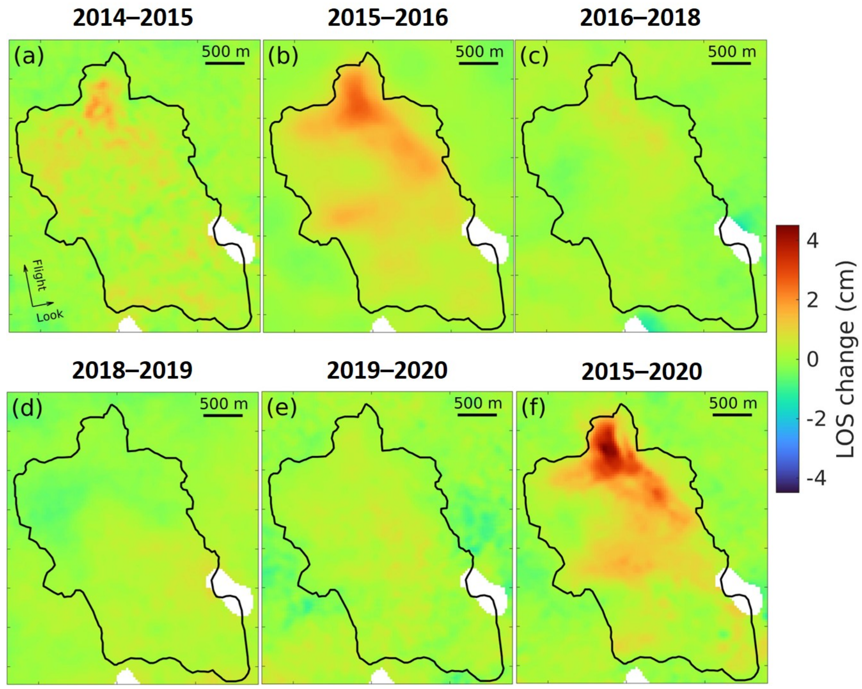

Figure 4. ALOS-2 interferograms indicating annual LOS displacement in (a) 2014–2015, (b) 2015–2016, (c) 2016–2018, (d) 2018–2019, (e) 2019–2020, and (f) 2015–2020. The detail of the dataset is listed in Table 1. Positive and negative values represent LOS lengthening and shortening.

4.3 Seasonal displacement by Sentinel-1 and validation with ALOS-2

Figure 5 shows stacked Sentinel-1 interferograms indicating seasonal LOS change for 2017–2020. The detail of the interferograms used in Figure 5 is shown in Table S1. In 2017–2018, the LOS lengthened by over 7 cm between May and August (early thawing season) in the north area (Figure 5a), but did not change between August and October (late thawing season; Figure 5b). On the contrary, the LOS shortened by up to 5 cm in the north area from October to December (early freezing season; Figure 5c). During December 2017–March 2018 (late freezing season), there was no LOS change with good coherence (Figure 5d). From 2018 to 2021, a similar pattern of seasonal LOS change was repeated. The LOS lengthened between May and August (early thawing season) in 2018, 2019, and 2020 by up to 5, 6.5, and 3.5 cm, respectively, in the north area (Figures 5e, 5i, and 5m). In the following period between August and October each year, there were no LOS changes (Figures 5f, 5j, and 5n). From October to December, the LOS shortened in 2018, 2019, and 2020 by up to 6, 2.5, and 1.3 cm, respectively, in the north area (Figures 5g, 5k, and 5o). In December–March, there was also no LOS change with good coherence (Figures 5h, 5l, and 5p). The spatial distributions of LOS shortening (Figures 5a, 5e, 5i, and 5m) and lengthening (Figures 5c, 5g 5k, and 5o) were almost comparable. However, the magnitude of the seasonal LOS lengthening/shortening was different each year, and it decreased secularly. Coherences of Sentinel-1 interferograms in thawing season, particularly from the end of March to the beginning of May every year, were significantly lost probably due to snowmelt, and surface displacements lacked in these periods. Thus, we should note that the total amount of seasonal thaw subsidence each year was uncertain.

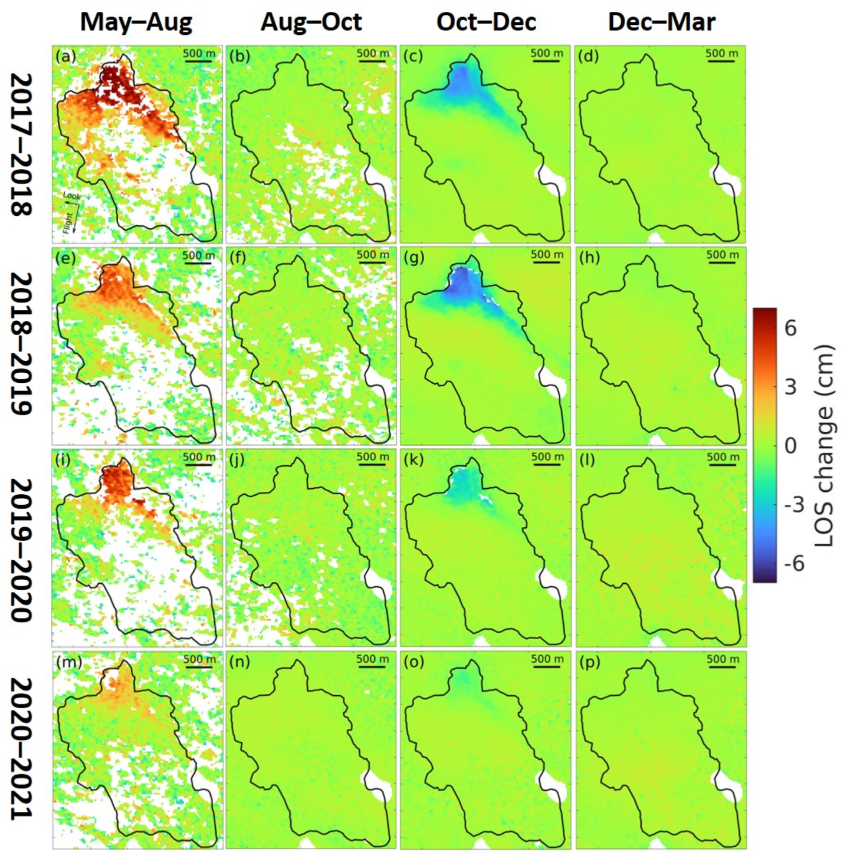

Figure 5. Stacked Sentinel-1 interferograms in the four periods (May–Aug, Aug–Oct, Oct–Dec, Dec–Mar) during 2017–2020. The detail of the dataset is listed in Table S1. Positive and negative values represent LOS lengthening and shortening.

Since there are no available in-situ data for validating our InSAR-based displacements, we performed cross-validated then using the corresponding ALOS-2 and Sentinel-1 InSAR data to assess the quality. Figure 6 shows an inter-comparison of LOS changes between ALOS-2 and Sentienl-1 during the thawing season in 2019 (Table 3). The ALOS-2 and Sentinel-1 interferograms in June and July 2019 show LOS lengthening of up to 3 cm with similar spatial pattern (Figures 6a and b). The mean difference between them, with standard deviation, is 0.0±0.8 cm. In the subsequent period of June and July 2019, the ALOS-2 and Sentinel-1 interferograms showed almost no displacement in the analysis area, with the mean difference being 0.0±0.7 cm. Although some Sentinel-1 interferograms in the thawing season did not show good coherence (Figures 6b and 6e), the validation results indicated that the ALOS-2 and Sentinel-1 interferograms could detect the same LOS displacements. Validation during the early winter season (using interferograms indicating frost heave) is desirable, but could not be performed due to the absence of ALOS-2 data in early winter over the study area.

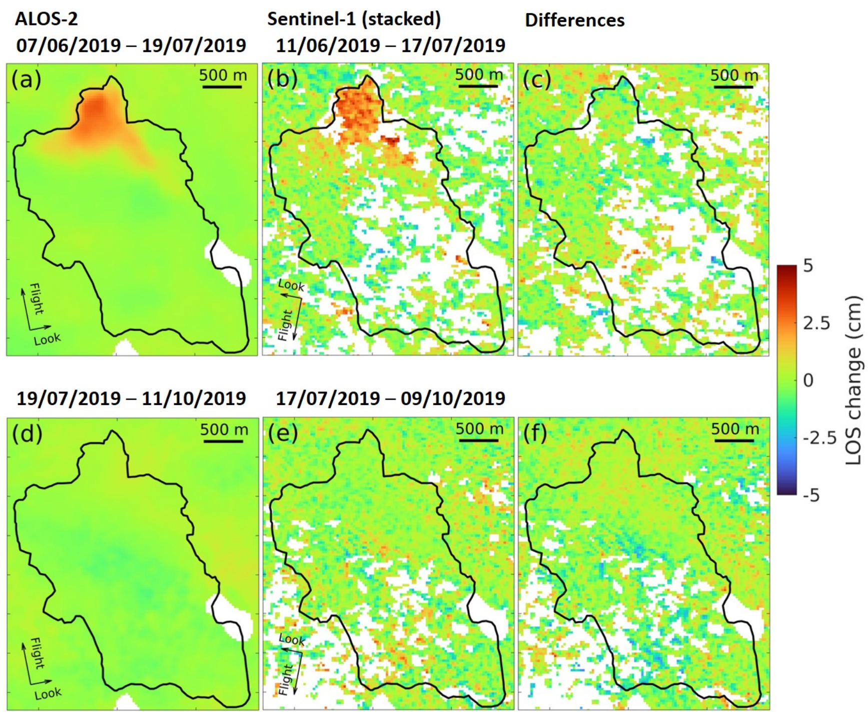

Figure 6. Comparison of LOS changes between (a and d) ALOS-2, (b and e) stacked Sentinel-1 interferograms, and (c and f) the differences of them in the two different periods. The detail of the dataset is listed in Table S1. Positive and negative values represent LOS lengthening and shortening.

4.4 Long-term displacement by ALOS-2 InSAR time-series analysis and estimation of thawed excess ice volume

Using generated 11 ALOS-2 interferograms (Figure 7a), we conducted SBAS-type time-series analysis to derive the cumulative displacement for 2014–2020. Figure 7b shows the spatial distribution of cumulative subsidence in the burned area between 2014 and 2020. The cumulative LOS displacement was projected onto the vertical subsidence with the assumption of no horizontal displacement.

The maximum subsidence occurred around P1 (up to 7 cm), followed by P2 (up to 4.5 cm). Temporal changes in subsidence at three points in the burned area (P1–P3) are shown in Figure 7c. The results indicate that major subsidence occurred by 2016 (~5 cm), followed by a few centimeters in the next four years. In 2019–2020, the magnitude of subsidence was greater than that in the previous year. In contrast, there was no cumulative displacement outside the scar at P4 (Figure 7c), indicating that the ground was stable.

From the temporal evolution of post-forest fire deformation data from October 2014 to July 2020 and the assumption that the long-term subsidence was caused by ground ice melting, we estimated the total thawed ice volume to be 0.11±0.2 km^3. The estimation error was calculated based on the root mean square of the no deformation signals outside the burned area (Figure 7a). The thawed ice thickness was 0.02 m km^{-2}. Since there was no deformation data immediately after the fire (2013–2014), the volume of thawed ice may be considered to be larger.

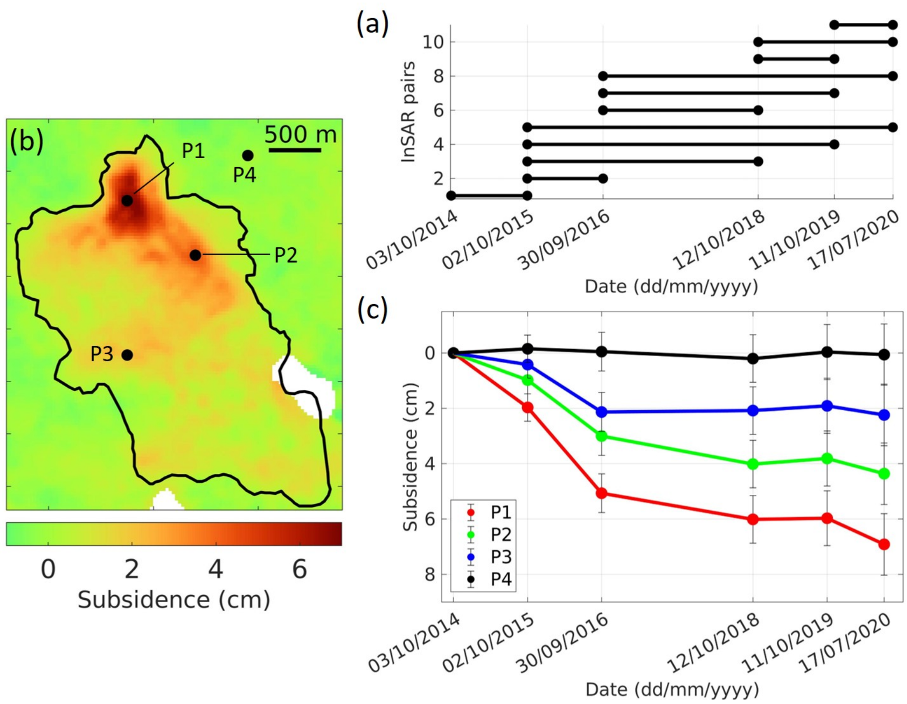

Figure 7. (a) Interferometric pairs used for the SBAS time-series analysis. (b) Cumulative subsidence map between October 2014 and July 2020 by the SBAS analysis using the dataset shown in (a). (c) Temporal changes in subsidence at P1–P4. P1–P3 are in the burned area, but P4 is outside..

4.5 Modeled seasonal thaw settlement and frost heave using air temperature and soil properties

Using the observed seasonal thaw settlement and frost heave data, we modeled the surface displacement using the method described in Section 3.4. Figure 8 shows the observed and modeled seasonal thaw settelement for 2017–2020. The observed data in Figure 5 are also projected onto the vertical displacement, similar to Figure 7. In 2017, the modeled subsidence in the northern burned area was up to 5 cm smaller than the observed subsidence (Figures 8a–8c). Similar differences were observed in 2018 (Figures 8d–8f) and 2019 (Figures 8g–8i), but the area of difference over 2 cm between the observed and modeled subsidence was smaller than that in 2017 (Figures 8f and i). In 2020, the modeled subsidence was equal to the observed subsidence (Figures 8j-8l).

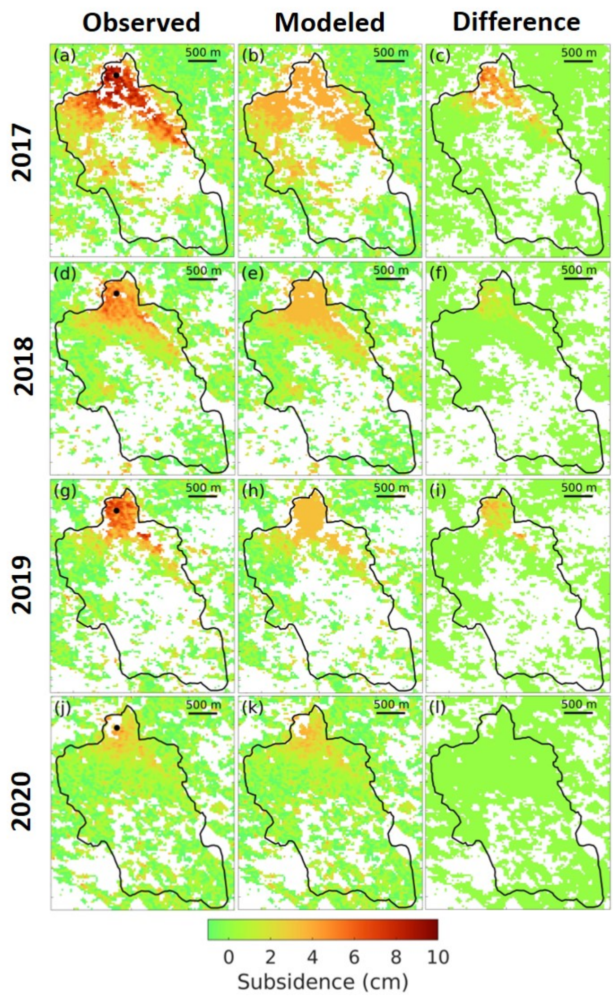

Figure 8. Observed and modeled yearly seasonal thaw settlement at 2017–2020. (a), (d), (g), and (j) represent the observed seasonal thaw settlement derived from the stacked Sentinel-1 interferograms shown in Fig 5a, 5e, 5i, and 5m,

respectively. (b), (e), (h), and (k) represent the thaw settlement modeled using Equation 3. (c), (h), (i), and (l) are the differences of them.

A similar analysis was conducted for frost heave. Figure 9 shows the observed and modeled frost heave during 2017–2020. Despite different parameter values (Table 4), we obtained a similar difference between the observed and modeled data, as shown in Figure 8. In 2017, the modeled uplift in the northern burned area was smaller than the observed uplift (Figures 9a and 9b). The difference was up to 2.5 cm (Figure 9c). A similar difference was observed in 2018, up to 3 cm, but the simulated uplift in 2019 and 2020 was almost equal to the observed uplift (Figures 9g–9l).

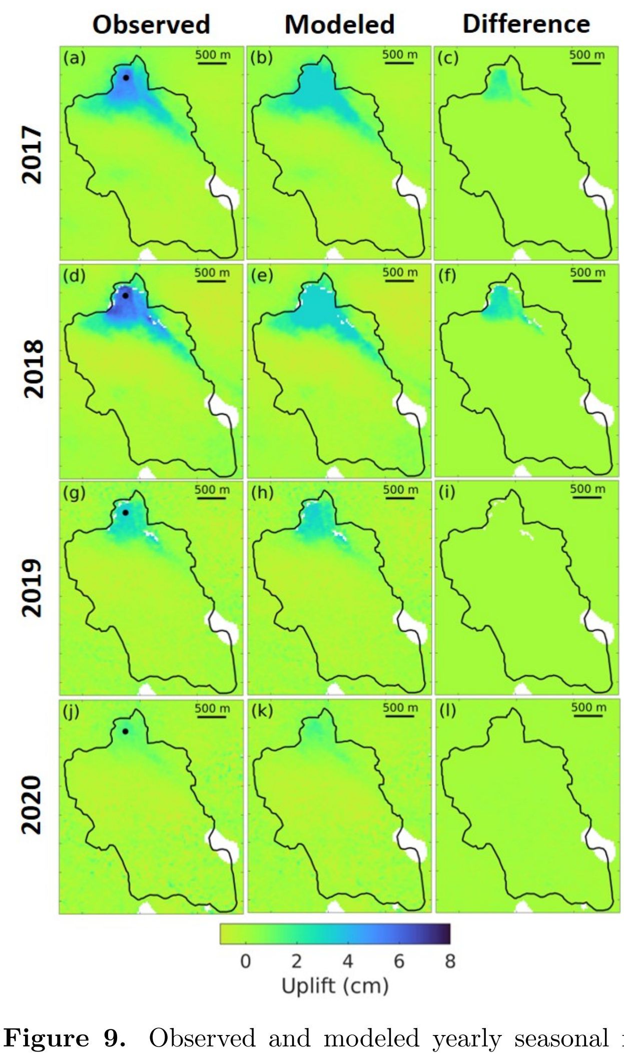

Figure 9. Observed and modeled yearly seasonal frost heave at 2017–2020. (a), (d), (g), and (j) represent the observed seasonal frost heave by the stacked

Sentinel-1 interferograms shown in Fig 5c, 5g, 5k, and 5o, respectively. (b), (e), (h), and (k) represent the frost heave modeled using Equation 3. (c), (h), (i), and (l) are the differences of them.

5 Discussion

5.1 Spatial variation of cumulative subsidence and burn severity

We compared the spatial variation in cumulative subsidence revealed by ALOS-2 (Figure 7b) with the burn severity associated with the 2013 forest fire (Figure 2a). Large subsidence areas (around P1 and P2 in Figure 7b) correspond to relateively high severity in the fire scar. This suggests that the high severity of dNBR reflects the degree of vegetation lost, including the organic layer, which led to deepening of ALT and permafrost thaw in the ground through changes in the albedo and water cycle through vegetation (Yoshikawa et al., 2003; Holloway et al., 2020). However, the distribution of cumulative subsidence did not exactly match that of severity. The burn severity of the area from P3 to the northwest in Figure 7b was moderate (Figure 2a), whereas the cumulative subsidence in this area was small (Figure 7b). This discrepancy was also observed in Batagay (Yanagiya & Furuya, 2020). In that case, they considered the relationship between subsidence and local landforms. Larger subsidence was observed in the east-facing slope, where thin active layers were likely to develop many gullies. In this study, a large subsidence occurred on the north-facing slope (Figure 2b), which corresponds to high burn severity. We have considered that the relatively larger amount of ground ice under the north-facing slope and the strong severities of the fire caused the significant subsidence.

The time-series plot of the cumulative subsidence (Figure 7c) revealed that major subsidence occurred in 2014 and 2016 within a few years after the fire. This temporal pattern was reported in some previous studies. Michaelides et al. (2019) showed that seasonal deformation was the maximum a few years after a fire event using event samples of wildfires in southwestern Alaska. Our time-series data also verified this pattern, with the annual subsidence decreasing until 2019. However, annual subsidence again increased in 2019–2020 from that in the previous year, even though the last SAR data was obtained in July, not September or October. This may reflect the intense heat in the spring of 2020. The number of wildfires in 2020 was much higher than that in other years (McCarty et al., 2020), which could promote permafrost thaw in the post-wildfire area. Long-term observations are needed to assess future permafrost stability.

5.2 Thawed excess ice volume and comparison of other forest fire cases

The estimated volume of thawed excess ice associated with the 2013 forest fire is 0.11 km^3, which is significantly smaller than in Batagay (Yanagiya & Furuya, 2020). The estimated excess ice loss in Batagay is 3.56 km^3, more than 30 times larger than in Mayya. Although the burned area was much larger in Batagay than in Mayya, the average thickness of ground ice melting in Batagay is about 0.1 m km^{-2}, five times as much as in Mayya. This is possibly due to the presence of massive ground ice in Batagay, which has been considered to be present through the investigation at Batagaika megaslump (Murton et al., 2017). Moreover, the study area of Batagay is located far north and at a higher altidude than Mayya, and ALT is considered to be small. Thus, the impact of wildfires on permafrost could be larger in Batagay than that in Mayya, causing large surface subsidence due to significant permafrost thaw. On the contrary, there is no information about the existence of ground ice in the fire scar in Mayya, and the ALT at disturbed areas in Mayya is large, up to 2–3 m. Therefore, the observed long-term subsidence of ~ 7 cm may be caused by ice-lens melting in the transient layer (Shur et al., 2005). Transitent layer thickness varies depending on the environmental conditions and landscape disturbance, with the thickness in disturbed areas of Central Yakutia being 0.1–0.3 m (Iijima and Fedorov, 2019). Assuming that the volumetric ice content in the transient layer was 40 % and the layer thawed after the fire, the estimated subsidence was 4–12 cm, which is reasonable for our observed data.

The details of the seasonal displacement in Figure 5 indicate that the seasonal thaw subsidence terminated in August and almost no displacement occurred in late summer (between August and October). Inter-annual subsidence caused by ground ice melting in northwestern Alaska was observed in late summer (Zwieback Meyer, 2021), and our data suggest that inter-annual subsidence had almost stopped since at least 2017, four years after the event. This corresponds to the results of the ALOS-2 time-series analysis (Figure 7c). In contrast, the seasonal thaw settlement in Batagay was greater than the frost heave in 2018, even four years after the event (Yanagiya & Furuya, 2020). The seasonal subsidence decreased in 2019, but the inter-annual subsidence may continue for a few years, which is longer than that in Mayya.

5.3 Comparison of observed seasonal displacement with vegetation and meteorological data

Although the Sentinel-1 interferograms revealed seasonal thaw settlement and frost heave in the post-forest fire area (Figures 5, 8, and 9), the magnitude of the displacements varied each year. We compared the magnitude of subsidence/uplift with temporal vegetation changes and meteorological data. Figure 10a shows a comparison of the displacement with NDVI. Immediately after the fire, the NDVI was almost 0 (Figure 3a). The NDVI in 2018, five years after the event, recovered to 0.37 (also see Figure 3d), and then the NDVI decreased to 0.23 in 2020. This temporal pattern was similar to that of the seasonal displacements. Due to the decrease of vegetation in the fire scar, evapotranspiration would become small and soil water content should get increased. On the contrary, the magnitude of seasonal displacements decreased. This indicates that the inter-annual changes in vegetation was not directly linked to the magnitude of seasonal displacements. A comparison of seasonal thaw settlement and frost heave indicated that the magnitude of frost heave in a year was close to that of thaw settlement in the subsequent year.

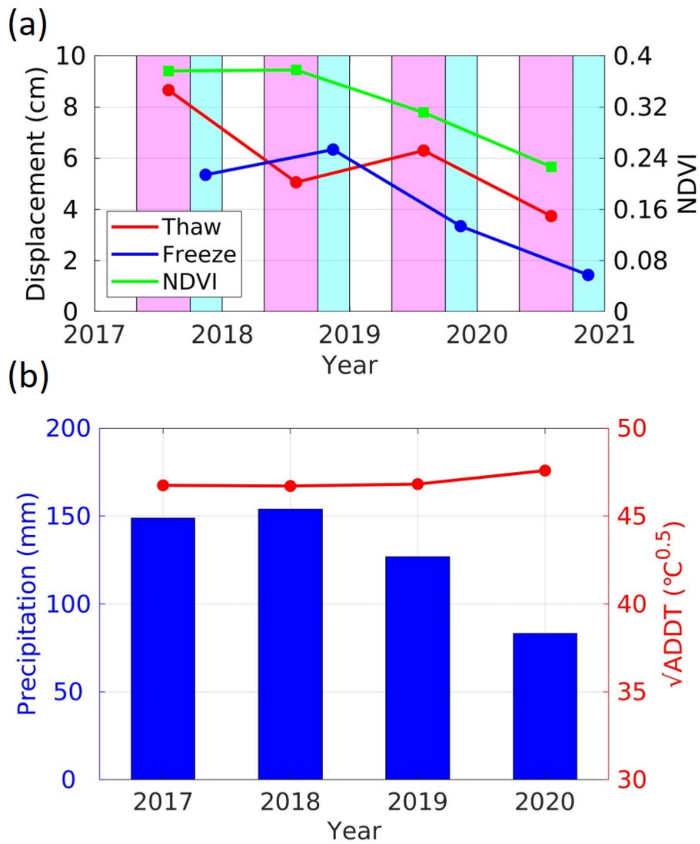

Figure 10. (a) Comparison among the magnitude of seasonal thaw settlement, frost heave, and NDVI in 2017–2020. Magenta and cyan hatches indicate thawing (April–September) and early freezing (October–December) seasons. (b) The blue bars show precipitation between May and October, and the red line shows the square root of the accumulated degree days of thawing (ADDT) in 2017–2020.

A comparison of the surface displacement with the air temperature and precipitation is shown in Figure 10b. The root of the ADDT between 2017 and 2020 was almost stable, and that in 2020 was slightly large, probably due to the intense heat in the 2020 spring season. However, the precipitation between May and October in 2017–2020 changed inter-annually; the precipitation in 2018 was slightly higher than that in 2017, but it decreased in 2019 and 2020. The pattern of the temporal change corresponds to that of the magnitude of frost heave (Figures 10a and 10b). This indicates that the magnitude of frost heave may be linked to precipitation during the thawing season. High precipitation during the thawing season increases the soil moisture, which has the potential to generate many ice lenses in early winter. Moreover, the observed uplift signal shows that frost heave stopped at the end of the year (Figures 5c, 5d, 5g, 5h, 5k, 5l, 5o, and 5p). One of the possible reasons is that the soil moisture in the active layer becomes completely frozen at the time; one of the alternatives is that unfrozen soil moisture stopped contributing to ice lens formation. No displacement in mid-winter was observed by Yanagina and Furuya (2020), despite the increase in the ADDF in the period. These observations indicate that the amount of water available to form ice lenses is important for causing frost heave, and that the temperature gradient instead of the temperature itself may be related to an ice lens generation. When many ice lenses are formed in an early freezing season, causing larger frost heave, the magnitude of subsidence in the next thawing season could be larger than that caused by the ice–water phase change.

5.4 Implication for geophysical modeling inferred from modeled seasonal displacement

InSAR-observed seasonal thaw settlement is sometimes assumed to be proportional to the square root of the ADDT, and the maximum subsidence occurs on or after the surface temperature returns to below freezing (Liu et al., 2012; Schaefer et al., 2015; Michaelides et al., 2019), which is based on the Stefan's equation. These studies assumed that subsidence occurred due to volumetric change from ice to water, and ALT was derived from the observed InSAR data. Our observed InSAR data showed that seasonal subsidence was completed at the beginning of August, even when the ADDT still increased (Figures 5a, 5e, 5i, and 5m). We considered that the seasonal subsidence could not be directly linked to the ADDT, but was associated with ice lens melting. Ice lenses are considered the main cause of frost heave. Taber (1930) showed that frost heave could not be explained by volumetric expansion due to phase change of pore water, and various studies have focused on frost heave mechanisms in recent decades (reviewed in Peppin Style, 2013). Yanagiya and Furuya (2020) concluded that the observed frost heave signals could be interpreted by 1-D premelting dynamics proposed by Rempel et al. (2004). Our InSAR data also showed significant frost heave in October–December (Figures 5c, 5g, 5k, and 5o), and no surface displacement was detected during mid-winter (Figures 5d, 5h, 5l, and 5p) when the ADDF continued to increase. The frost heave rate in November 2018 was apporiximately 1.7×10^{-8} m s^{-1}, which is similar to that reported by Yanagiya and Furuya (2020). This implies that our data supports their conclusions.

We also simulated seasonal thaw settlement and frost heave data using various soil parameters and air temperature data (Figure 11). Compared with the observed thaw settlement in 2017 (magenta line with markers in Figure 11a), the simulated subsidence with default parameters (solid black line) used in Figure 8 was smaller in the corresponding period. Even with 60% volumetric water content, the simulated result (black dotted line) was smaller than the observed one. Two other sets of parameters with different values of thermal conductivity and soil bulk density were tested (red and blue lines), which showed that the simulated data did not match the observed ones. Similar results were obtained for the seasonal frost heave in 2018 (Figure 11b). Simulated uplifts with various parameters did not explain the observed uplift.

These simulations may also indicate that the Stefan's equation with plausible soil parameters and volume change associated with ice–water phase change is not sufficient to quantitatively explain the observed seasonal displacements. Our results show that at least two-fold more than the simulated result is needed to explain the observed large surface displacement of over 5 cm, such as the subsidence in 2017 and the uplift in 2018. Recent in-situ observations reported by Yanagiya (2022) showed that localized thaw settlement within fire scars does not necessarily correlate with ALT. Our simulation results may support his findings. Furthermore, the temporal changes in the observed and simulated seasonal displacements, particularly the peak of the displacement gradient, significantly differ from each other (Figures 11a and b). This implies that the phase change expansion model does not explain seasonal displacement onset/end or amount. The ice lens formation reported by Rempel et al. (2004) could explain the InSAR frost heave signal as reported by Yanagiya and Furuya (2020). However, the calculation requires many parameters, such as pore water pressure and the hydraulic conductivity of frozen fringes, many of which are difficult to be measured in the field (Chen et al., 2020).

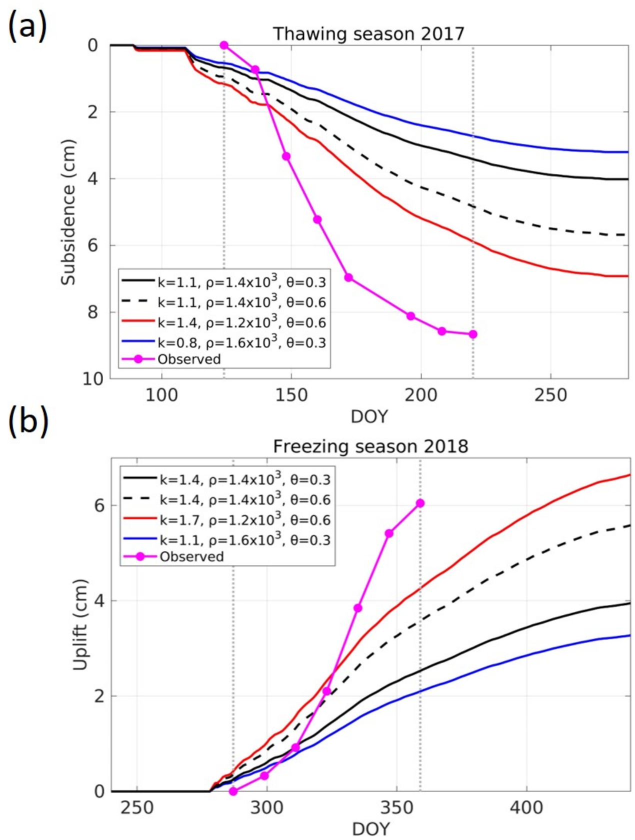

Figure 11. Simulated seasonal (a) thaw settlement in 2017 and (b) frost heave in 2018 with various soil parameters and temperature data. Different line styles represent the different parameters used. The Sentinel-1-observed displacements are also plotted in magenta lines with markers.

The discrepancies between the observed and simulated seasonal displacements may be solved using a model based on the ice segregation theory. Konrad and Morgenstern (1981) proposed a segregation potential model to address problems, in which requires many essential parameters for the calculation. The segregation potential is expressed as a function of the pore water pressure at the base of the ice lens. One of the significant advantages of the model is that it can be used to calculate frost heave when the temperature is measured. Zhang et al. (2020) successfully applied this model to a series of one-sided frost heave tests under external pressure in a closed system. Such a model may explain our observed frost heave signals if the temperature gradient and pore water pressure are known. It should be noted that there is a possibility that the significant differences between the soil parameters used and in-situ in our simulations cannot explain the observed displacement. The theoretical mechanisms of frost heave still remain open questions, and more simulations and in-site observations are needed.

Our multi-year seasonal displacement data are useful for better understanding the freeze–thaw dynamics in Central Yakutia. However, even 12 days spanning the Sentinel-1 interferograms did not capture the entire seasonal thaw settlement due to low coherence during snowmelt in April and May. Therefore, the seasonal thaw settlement in our data did not completely correspond to the entire thaw settlement. To capture this, future L-band SAR missions, such as ALOS-4 and NISAR, are expected in view of high-frequency observations in permafrost regions, which could derive both seasonal and inter-annual displacement. Such observation data will help to understand permafrost dynamics and predict the future state of permafrost regions.

6 Conclusion

Forest fires can enhance abrupt permafrost degradation. However, the temporal variation of surface deformation due to permafrost thaw in the post forest fire area remains uncertain due to insufficient observation data. This study examined inter-annual and seasonal displacement associated with freeze–thaw dynamics in a forest fire scar in Eastern Siberia, Russia, using InSAR analysis with ALOS-2 L-band and Sentinel-1 C-band SAR data. InSAR time-series analysis using ALOS-2 data revealed up to 7 cm inter-annual subsidence from October 2014 to July 2020, which was presumably caused by melting ice lens in the transient layer. Stacked Sentinel-1 InSAR images from 2017 to 2021 revealed seasonal displacements associated with seasonal thaw settlement and frost heave. The magnitude of the seasonal displacements varied yearly, but the temporal change in frost heave corresponded to that in precipitation during the thawing season from 2017 to 2020. This suggests that precipitation amount during the thawing season is associated with the magnitude of ice lens formation in soil. We modeled the seasonal thaw settlement and frost heave uplift using the Stefan's equation and the difference in density between ice and water, with some assumptions. The modeled results show that the observed seasonal displacements could not be explained using this model quantitatively, implying that a new model associated with ice lens formation and thawing must be considered to explain the observed seasonal displacement.

Acknowledgments

This study was initially conducted under the ALOS-2 application research in Earth Observation Research Center (EORC) in JAXA when TA was affiliated to JAXA. This study was supported by the Arctic Challenge for Sustainability Research Projects II (JPMXD1420318865), funded by the Ministry of Education, Culture, Sports, Science, and Technology of Japan. This study was also supported by the Grant for Joint Research Program of the Japan Arctic Research Network Center (FS04), JSPS KAKENHI (18H03353), Joint Research Program of Earthquake Research Institute, the University of Tokyo (2021-B-03), and the Environment Research and Technology Development Fund project (2-1605) by the Ministry of Environment and the Environmental Restoration and Conservation Agency. The ALOS-2 and Sentinel-1 data used in this study are copyrighted by JAXA and the European Space Agency, respectively. We thank Shunji Kanie, Takumi Kawamura, Masato Furuya, Kazuki Yanagiya, and Masato Tanaka for their valuable comments.

Data availability statement

ALOS-2 data are shared among the PALSAR Interferometry Consortium to Study our Evolving Land Surface (PIXEL), and provided from JAXA under a cooperative research contract with JAXA. Sentinel-1 data were downloaded from the Copernicus Open Access Hub (https://scihub.copernicus.eu/). AW3D30 data was downloaded from the ALOS Research and Application Project at the EORC on the JAXA website (https://www.eorc.jaxa.jp/ALOS/a/en/dataset/aw3d30/aw3d30_e.htm). Landsat images were downloaded from the United States Geological Survey EarthExplorer (http://earthexplorer.usgs.gov). The meteorological data of Yakutsk were downloaded from the National Centers for Environmental Information of National Oceanic and Atmospheric Administration. Figures were generated using Generic Mapping Tools (GMT) software (Wessel et al., 2013) and commercial MATLAB software developed by MathWorks (https://www.mathworks.com/).

References

Abe, T., Iwahana, G., Efremov, P.V., Desyatkin, A.R., Kawamura, T., Fedorov, A., Zhegusov, Y., et al. (2020). Surface displacement revealed by L-band InSAR analysis in the Mayya area, Central Yakutia, underlain by continuous permafrost. *Earth Planets Space*, 72, 138. https://doi.org/10.1186/s40623-020-01266-3

Antonova, S., Sudhaus, H., Strozzi, T., Zwieback, S., Kääb, A., Heim, B., Langer, M., et al. (2018). Thaw Subsidence of a Yedoma Landscape in Northern Siberia, Measured In situ and Estimated from TerraSAR-X Interferometry. *Remote Sensing*, 10(4), 494. https://doi.org/10.3390/rs10040494

Berardino, P., Fornaro, G., Lanari, R., & Sansosti, E. (2002). A new algorithm for surface deformation monitoring based on small baseline differential SAR Interferograms. *IEEE Transactions on Geoscience and Remote Sensing*, 40(11), 2375–2383. https://doi.org/10.1109/TGRS.2002.803792

Biggs, J., Wright, T., Lu, Z., & Parsons, B. (2007). Multi-interferogram method for measuring interseismic deformation: Denali Fault, Alaska. *Geophysical Journal International*, 170(3), 1165–1179. https://doi.org/10.1111/j.1365-246X.2007.03415.x

Bosikov, N. P. (1991). Alas Evolution of Central Yakutia. Yakutsk Permafrost Institute SD USSR AS. (In Russian)

Brown, J., Ferrians, O., Heginbottom, J., & Melnikov, E. (2002). Circum-Arctic Map of Permafrost and Ground-ice Conditions, Version 2. National Snow and Ice Data Center, Boulder, Colorado, USA. https://doi.org/10.7265/skbg-kf16

Chen, J., Liu, L., Zhang, T., Cao, B., & Lin, H. (2018). Using persistent scatterer interferometry to map and quantify permafrost thaw subsidence: A case study of Eboling Mountain on the Qinghai-Tibet Plateau. *Journal of Geophysical Research: Earth Surface*, 123, 2663–2676. https://doi.org/10.1029/2018JF004618

Chen, L. and Zhang, X.Y. (2020). A model for predicting the hydraulic conductivity of warm saturated frozen soil. *Building and Environment*, 179, 106939. https://doi.org/10.1016/j.buildenv.2020.106939

Costantini, M. (1998). A novel phase unwrapping method based on network programming. *IEEE Trans Geoscience and Remote Sensing*, 36, 813–821.

Czudek, T., & Demek, J. (1970). Thermokarst in Siberia and its influence on the development of lowland relief. *Quaternary Research*, 1(1), 103-120. https://doi.org/10.1016/0033-5894(70)90013-X

Daout, S., Doin, M.-P., Peltzer, G., Socquet, A., & Lasserre, C. (2017). Large-scale InSAR monitoring of permafrost freeze-thaw cycles on the Tibetan Plateau. *Geophysical Research Letters*, 44, 901–909. https://doi.org/10.1002/2016GL070781

Desyatkin, A., Fedorov, P., Filippov, N., & Desyatkin, R. (2021). Climate Change and Its Influence on the Active Layer Depth in Central Yakutia. *Land*, 10(1), 3. https://dx.doi.org/10.3390/land10010003

Desyatkin, R., Filippov, N., Desyatkin, A., Konyushkov, D., & Goryachkin, S. (2021). Degradation of Arable Soils in Central Yakutia: Negative Consequences of Global Warming for Yedoma Landscapes, *Frontiers in Earth Science*, 9, 683730. https://doi.org/10.3389/feart.2021.683730

Fedorov, A. N., Gavriliev, P.P., Konstantinov, P. Y., Hiyama, T., Iijima, Y., & Iwahana, G. (2014). Estimating the water balance of a thermokarst lake in the middle of the Lena River basin,

eastern Siberia. *Ecohydrology*, 7, 188–196. https://doi.org/10.1002/eco.1378

Fedorov, A. N., Iwahana, G., Konstantinov, P. Y., Machimura, T., Argunov, R. N., Efremov, P. V., Lopez, L. M. C., et al. (2017). Variability of Permafrost and Landscape Conditions Following Clear Cutting of Larch Forest in Central Yakutia, *Permafrost and Periglacial Processes*, 28, 331–338. https://doi.org/10.1002/ppp.1897

French, H. M. (2017). The periglacial environment, 4th edn. Wiley, West Sussex

Gibson, C. M., Chasmer, L. E., Thompson, D. K., Quinton, W. L., Flannigan, M. D., & Olefeldt, D. (2018). Wildfire as a major driver of recent permafrost thaw in boreal peatlands. *Nature Communications*, 9(1), 3041. https://doi.org/10.1038/s41467-018-05457-1

Goldstein, R. M., & Werner, C. L. (1998). Radar interferogram filtering for geophysical application. *Geophysical Research Letters*, 25, 4035–4038. https://doi.org/10.1029/1998GL900033

Hanssen, R. F. (2001). Radar Interferometry: Data interpretation and error analysis. Kluwer Academic Press.

Holloway, J. E., Lewkowicz, A. G., Douglas, T. A., Li, X., Turetsky, M .R., Baltzer J.L., & Jin, H. (2020). Impact of wildfire on permafrost landscapes: A review of recent advances and future prospects. *Permafrost and Periglacial Processes*, 31, 371–382. https://doi.org/10.1002/ppp.2048

Hu, Y., Liu, L., Larson, K. M., Schaefer, K. M., Zhang, J., & Yao, Y. (2018). GPS Interferometric Reflectometry reveals cyclic elevation changes in thaw and freezing seasons in a permafrost area (Barrow, Alaska). *Geophysical Research Letters*, 45, 5581–5589. https://doi.org/10.1029/2018GL077960

Iijima, Y, Fedorov, A. N., Park, H., Suzuki, K., Yabuki, H., Maximov, T. C., & Ohata, T. (2010). Abrupt increase in soil temperature under conditions of increased precipitation in a permafrost region, the central Lena River basin. *Permafrost and Periglacial Processes*, 21, 30–41. https://doi.org/10.1002/ppp.662

Iijima, Y., Park, H., Konstantinov, P. Y., Pudov, G. G., & Fedorov, A. N. (2017). Active-Layer Thickness Measurements Using a Handheld Penetrometer at Boreal and Tundra Sites in Eastern Siberia. *Permafrost and Periglacial Processes*, 28, 306–313. https://doi.org/10.1002/ppp.1908

Iijima, Y., & Fedorov A. N. (2019). Permafrost-Forest Dynamics. In T. Ohta, T. Hiyama, Y. Iijima, A. Kotani, & T. C. Maximov (Eds.), *Water-Carbon Dynamics in Eastern Siberia*, pp309, Springer Singapore.

Iijima, Y., Abe, T., Saito, H., Ulrich, M., Fedorov, A. N., Basharin, N. I., Gorokhov, A. N., et al. (2021). Thermokarst Landscape Development Detected by Multiple-Geospatial Data in Churapcha, Eastern Siberia. *Frontiers in Earth Science*, 9, 750298. https://doi.org/10.3389/feart.2021.750298

Iwahana, G., Machimura, T., Kobayashi, Y., Fedorov, A.N., Konstantinov, P. Y., & Fukuda, M. (2005). Influence of forest clear-cutting on the thermal and hydrological regime of the active layer near Yakutsk, eastern Siberia. *Journal of Geophysical Research*, 110, G02004. https://doi.org/10.1029/2005JG000039

Iwahana, G., Uchida, M., Liu, L., Gong, W., Meyer, F. J., Guritz, R., Yamanokuchi, T., et al. (2016). InSAR Detection and Field Evidence for Thermokarst after a Tundra Wildfire, Using ALOSPALSAR. *Remote Sensing*, 8(3), 218. https://doi.org/10.3390/rs8030218

Karunaratne, K. C., & Burn, C. R. (2003). Freezing n-factors in discontinuous permafrost terrain, Takhini River, Yukon Territory, Canada. In Phillips, M., Springman, S. M., Arenson, L. U., eds., *Proceedings of Eighth International Conference on Permafrost*, 21-25 July 2003, Zurich Switzerland. Balkema, Lisse, 1, 519-524.

Key, C. H., & Benson, N. C. (2006). Landscape assessment: Sampling and analysis methods. In *FIREMON: Fire Effects Monitoring and Inventory System, General Technical Report* (Vol. RMRS-GTR-164, pp. LA-1–55). Fort Collins, CO: Department of Agriculture, Forest Service, Rocky Mountain Research Station. https://doi.org/10.2737/RMRS-GTR-164

Klene, A. E., Nelson, F. E., Shiklomanov, N. I., & Hinkel, K. M. (2001). The N-factor in Natural Landscapes: Variability of Air and Soil-Surface Temperatures, Kuparuk River Basin, Alaska, USA. *Arctic, Antarctic, and Alpine Research*, 33(2), 140–148. https://doi.org/10.2307/1552214

Konrad, J. M., & Morgenstern, N. R. (1981). The segregation potential of a freezing soil. *Canadian Geotechnical Journal*, 18(4), 482–491. https://doi.org/10.1139/t81-059

Kornei, K. (2020). Wildfires trigger long-term permafrost thawing. *EOS*, 101. https://doi.org/10.1029/2020EO148336

Liu, L., Jafarov, E. E., Schaefer, K. M., Jones, B.M., Zebker,H. A., Williams, C. A., Rogan, J., et al. (2014). InSAR detects increase in surface subsidence caused by an Arctic tundra fire. *Geophysical Research Letters*, 41, 3906–3913. https://doi.org/10.1002/2014GL060533

Liu, L., Schaefer, K. M., Chen, A. C., Gusmeroli, A., Zebker, H. A., & Zhang, T. (2015). Remote sensing measurements of thermokarst subsidence using InSAR. *Journal of Geophysical Research: Earth Surface*, 120, 1935–1948. https://doi.org/10.1002/2015JF003599

Liu, L., Schaefer, K., Zhang, T. & Wahr, J. (2012). Estimating 1992–2000 average active layer thickness on the Alaskan North Slope from remotely sensed surface subsidence, *Journal of Geophysical Research*, 117, F01005. https://doi.org/10.1029/2011JF002041

Liu, L., Zhang, T., & Wahr, J. (2010). InSAR measurements of surface deformation over permafrost on the North Slope of Alaska. *Journal of Geophysical Research*, 115, F03023. https://doi.org/10.1029/2009JF001547

Lunardini, V. (1978). Theory of n-factors and correlations of data, In *Proceedings of the Third International Conference on Permafrost*, 10-13 July 1978, Edmonton, Alberta, Canada, 1, 40–46.

Mack, M. C., Bret-Harte, M. S., Hollingsworth, T. N., Jandt, R. R., Schuur, E. A. G., Shaver, G. R., & Verbyla, D. L. (2011). Carbon loss from an unprecedented Arctic tundra wildfire. *Nature*, 475(7357), 489–492. https://doi.org/10.1038/nature10283

McCarty, J. L., Smith, T. E. L. & Turetsky, M. R. (2020). Arctic fires re-emerging. *Nature Geoscience*, 13, 658–660. https://doi.org/10.1038/s41561-020-00645-5

Menne, M. J., Durre, I., Korzeniewski, B., McNeal, S., Thomas, K., Yin, X., Anthony, S., Ray, et al. (2012). Global Historical Climatology Network - Daily (GHCN-Daily), Version 3. NOAA National Climatic Data Center, doi:10.7289/V5D21VHZ

Menne, M. J., Durre, I., Vose, R. S., Gleason, B. E., & Houston, T. G. (2012). An Overview of the Global Historical Climatology Network-Daily Database. *Journal of Atmospheric and Oceanic Technology*, 29, 897-910. doi:10.1175/JTECH-D-11-00103

Michaelides, R. J., Zebker, H. A., Schaefer, K., Parsekian, A., Liu, L., Chen, J., Natali, S., et al. (2019). Inference of the impact of wildfire on permafrost and active layer thickness in a discontinuous permafrost region using the remotely sensed active layer thickness (ReSALT) algorithm. *Environmental Research Letters*, 14(3), 035007. https://doi.org/10.1088/1748-9326/aaf932

Miller, J. D., & Thode, A. E. (2007). Quantifying burn severity in a heterogeneous landscape with a relative version of the delta Normalized Burn Ratio (dNBR). *Remote Sensing of Environment*, 109(1), 66–80. https://doi.org/10.1016/j.rse.2006.12.006

Molan, Y. E., Kim, J. W., Lu, Z., Wylie, B., & Zhu, Z. (2018). Modeling wildfire-induced permafrost deformation in an Alaskan boreal Forest using InSAR observations. *Remote Sensing*, 10(3), 405. https://doi.org/10.3390/rs10030405

Murton, J. B., Edwards,M. E., Lozhkin, A. V., Anderson, P. M., Savvinov, G. N., Bakulina, N., Bondarenko, O. V., et al. (2017). Preliminary paleoenvironmental analysis of permafrost deposits at Batagaika megaslump, Yana Uplands, northeast Siberia. *Quaternary Research*, 87(2), 314–330. https://doi.org/10.1017/qua.2016.15

Natsuaki, R., Nagai, H., Motohka, T., Ohki, M., Watanabe, M., Thapa, R. B., Tadono, T., et al. (2016). SAR interferometry using ALOS-2 PALSAR-2 data for the Mw 7.8 Gorkha, Nepal earthquake. *Earth Planets Space*, 68, 15. https ://doi.org/10.1186/s4062 3-016-0394-4

Peppin, S. S. L., & Style, R. W. (2013). The Physics of Frost Heave and Ice-Lens Growth. *Vadose Zone Journal*, 12(1), 1-12. https://doi.org/10.2136/vzj2012.0049

Rempel, A. W., Wettlaufer, J. S., & Worster, M. G. (2004). Premelting dynamics in a continuum model of frost heave. *Journal of Fluid Mechanics*, 498, 227–244. https://doi.org/10.1017/S0022112003006761

Romanovsky, V. E., & Osterkamp, T. E. (2000). Effects of unfrozen water on heat and mass transport processes in the active layer and permafrost. *Permafrost and Periglacial Processes*, 11, 219–239. https://doi.org/10.1002/1099-1530(200007/09)11:3<219::aidppp352>3.0.co; 2–7

Rouyet, L., Lauknes, T. R., Christiansen, H. H., Strand, S. M., & Larsen, Y. (2019). Seasonal dynamics of a permafrost landscape, Adventdalen, Svalbard, investigated by InSAR. *Remote Sensing of Environment*, 231, 111236. https://doi.org/10.1016/j.rse.2019.111236

Schaefer, K., Liu, L., Parsekian, A., Jafarov, E., Chen, A., Zhang, T., Gusmeroli, A., et al (2015). Remotely Sensed Active Layer Thickness (ReSALT) at Barrow, Alaska using interferometric synthetic aperture radar, *Remote Sensing*, 7(4), 3735–3759. https://doi.org/10.3390/rs70403735

Schmidt, D. A., & Bürgmann, R. (2003). Time-dependent land uplift and subsidence in the Santa Clara valley, California, from a large interferometric synthetic aperture radar data set. *Journal of Geophysical Research*, 108(B9), 2416. https://doi.org/10.1029/2002JB002267

Schuur, E. A. G., McGuire, A. D., Schädel, C., Grosse, G., Harden, J. W., Hayes, D. J., Hugelius, G., et al. (2015). Climate change and the permafrost carbon feedback. *Nature*, 520(7546), 171–179. https://doi.org/10.1038/nature14338

Short, N., Brisco, B., Couture, N., Pollard, W., Murnaghan, K., & Budkewitsch, P. (2011). A comparison of TerraSAR-X, RADARSAT-2 and ALOS-PALSAR interferometry for monitoring permafrost environments, case study from Herschel Island, Canada. *Remote Sensing Environment*, 115(12), 3491–3506. https://doi.org/10.1016/j.rse.2011.08.012

Shur, Y., Hinkel, K. M., & Nelson, F. E. (2005). The transient layer: implications for geocryology and climate-change science. *Permafrost and Periglacial Processes*, 16, 5–17, https://doi.org/10.1002/ppp.518,2005.

Soloviev, P. A. (1959). Cryolithic zone of the Northern Part of Lena-Amga Interfluve, Izdatel'stvo Akademii SSSR. (in Russian)

Stefan, J. (1891). Über die theorie der eisbildung, insbesondere über die eisbildung im polarmeere, *Annalen der Physik*, 278(2), 269–286. (in German)

Strozzi, T., Antonova, S., Günther, F., Mätzler, E., Vieira, G., Wegmüller, U., Westermann, S., et al. (2018). Sentinel-1 SAR Interferometry for Surface Deformation Monitoring in Low-Land Permafrost Areas. *Remote Sensing*, 10(9), 1360. https://doi.org/10.3390/rs10091360

Taber, S. (1930). The Mechanics of Frost Heaving. *Journal of Geology*, 38(4), 303–317. https://doi.org/10.1086/623720

Takaku, J., Tadono, T., Doutsu, M., Ohgushi, F., & Kai, H. (2020). Updates of 'AW3D30' ALOS Global Digital Surface Model with Other Open Access Datasets. *The International Archives of the Photogrammetry, Remote Sensing and Spatial Information Sciences*, ISPRS, Vol.XLIII-B4-2020, 183–189. https://doi.org/10.5194/isprs-archives-XLIII-B4-2020-183-2020

Ulrich, M., Grosse, G., Strauss, J., & Schirrmeister, L. (2014). Quantifying Wedge-Ice Volumes in Yedoma and Thermokarst-Basin Deposits. *Permafrost and Periglacical Processes*, 25, 151–161. https://doi.org/10.1002/ppp.1810

Ulrich, M., Matthes, H., Schirrmeister, L., Schütze, J., Park, H., Iijima, Y., & Fedorov A. N. (2017). Differences in behavior and distribution of permafrost-related lakes in Central Yakutia and their response to climatic drivers. *Water Resource Research*, 53, 1167–1188. https://doi.org/10.1002/2016WR019267

United States Geological Survey (2003). Preliminary Assessment of the Value of Landsat 7 ETM+ Data following Scan Line Corrector Malfunction. https://d9-wret.s3.us-west-2.amazonaws.com/assets/palladium/production/s3fs-ublic/atoms/files/SLC_off_Scientific_U Accessed April 25 2022

van Everdingen, R. O. (2005). Multi-language glossary of permafrost and related ground-ice terms. International Permafrost Association. 2005. http://globalcryospherewatch.org/reference/gloss ary_docs/Gloss ary_of_Permafrost and_Ground-Ice_IPA_2005.pdf. Accessed Jan 23 2022

Wang, L, Marzahn. P., Bernier, M., Jacome, A., Poulin, J., & Ludwig, R. (2017). Comparison of TerraSAR-X and ALOS PALSAR Differential Interferometry With Multisource DEMs for Monitoring Ground Displacement in a Discontinuous Permafrost Region. *IEEE Journal of Selected Topics in Applied Earth Observations and Remote Sensing*, 10(9), 4074–4093. https://doi.org/10.1109/JSTARS.2017.2707337

Wegmüller, U., & Werner, C. L. (1997). Gamma SAR processor and interferometry software. In *Proceedings of the 3rd ERS Symposium*. 14-21 March 1997, Florence, Italy, 414, 1687–1692.

Wessel, P., Smith, W. H. F., Scharroo, R., Luis, J. & Wobbe, F. (2013) Generic mapping tools: improved version released. *EOS Trans AGU*, 94, 409–410. https://doi.org/10.1002/2013EO450001

Yanagiya, K. (2022). Abrupt permafrost thaw processes after wildfire revealed by InSAR and on-site observations at Batagay, Northeastern Siberia, *Ph. D. thesis at Hokkaido University*, Japan.

Yanagiya, K., & Furuya, M. (2020). Post-wildfire surface deformation near Batagay, Eastern Siberia, detected by L-band and C-band InSAR. *Journal of Geophysical Research: Earth Surface*, 125, e2019JF005473. https://doi.org/10.1029/2019JF005473

Yershov, E. D. (1998). *General Geocryology*. Cambridge University Press. https://doi.org/10.1017/CBO9780511564505

Yoshikawa, K., Bolton,W. R., Romanovsky, V. E., Fukuda, M., & Hinzman, L. D. (2003). Impacts of wildfire on the permafrost in the boreal forests of interior Alaska. *Journal of Geophysical Research*, 108, 8148. https://doi.org/10.1029/2001JD000438

Zhang, X., Sheng, Y., Huang, L., Huang, X., & He, B. (2020). Application of the Segregation Potential Model to Freezing Soil in a Closed System. *Water*, 12, 2418. https://doi.org/10.3390/w12092418

Zhang, Y., Wolfe, S. A., Morse, P. D., & Fraser, I. O. R. H. (2015). Spatiotemporal impacts of wildfire and climate warming on permafrost across a subarctic region, Canada. *Journal of Geophysical Research: Earth Surface*, 120, 2338–2356. https://doi.org/10.1002/2015JF003679

Zwieback, S., & Meyer, F. J. (2021). Top-of-permafrost ground ice indicated by remotely sensed late-season subsidence, *The Cryophere*, 15, 2041-2055. https://doi.org/10.5194/tc-15-2041-2021